Pressurizing magma within heterogeneous crust: a case study at the Socorro Magma Body, New Mexico, USA

Grant A. Block[1], Mousumi Roy[1], Emily Graves[2], Ronni Grapenthin[2]

[1]Department of Physics and Astronomy, University of New Mexico, 210 Yale Blvd NE, Albuquerque, 87131, NM, USA.

[2]Geophysical Institute and Department of Geoscience, University of Alaska, 2156 Koyukuk Drive, Fairbanks, 99775, AK, USA.

Key Points:

- InSAR confirms coeval subsidence and uplift (a so-called "sombrero" deformation pattern) persisted for > 100 years at the Socorro Magma Body
- A compliant region, modeled as a viscoelastic body surrounding a sill, is able to reproduce both the pattern and duration of deformation.
- Viscoelastic deformation within a broad compliant region supports the presence of mush zones at SMB and other mid-crustal magma bodies.

This manuscript has been submitted to Geophysical Research Letters for review. It has not yet been peer reviewed.

Corresponding author: Grant A. Block, `gblock@unm.edu`

Abstract

Surface deformation measurements play a key role in illuminating magma transport systems at active volcanic systems, however, unambiguous separation of deep and shallow transport remains elusive. The Socorro Magma Body (SMB) lacks an upper crustal magma transport system, allowing us to link geodetic measurements with predictions of numerical models investigating material/rheologic heterogeneities and magma-mush interaction in the mid-/lower crust. New InSAR observations confirm that a pattern of central surface uplift surrounded by a region of subsidence (previously coined "sombrero" deformation) has persisted over >100 yrs at the SMB. Our models suggest this pattern may reflect the presence of a large ($>$ 100 km width), weaker-than-ambient, compliant region surrounding the mid-crustal magma body. Interactions between the pressurizing sill-like magma body and the compliant region drive circulatory motions that manifest the sombrero pattern, depending on both viscoelastic relaxation and pressurization timescales, explaining its rare observation and transient nature.

Plain Language Summary

Magma in the crust is transported and stored within magma bodies (regions that are mostly liquid magma) and "mush" (mostly solid crystals and some liquid magma). Mush zones are thought to be too viscous to be erupted but are likely to be weaker than the surrounding rock. To understand volcanic eruptions, it is important to understand the distribution of magma and mush, and their mutual interactions. Here we study these interactions in a mid-crustal magma body, the Soccorro Magma Body (SMB), that does not have a surface volcano. Surface deformation at the SMB helps us study magma-mush interaction, especially in the mid-/lower crust. Previous surface deformation measurements at the SMB show "sombrero" deformation: a central area of uplift surrounded by a ring of subsidence. New satellite radar measurements are consistent with the previously reported pattern, confirming that this deformation remained remarkably constant through nearly 100 years. We suggest this is due to a large weak, mush region surrounding the SMB. Our computer models reproduce a long-lasting, consistent sombrero deformation pattern depending on mush properties as well as pressurization history of the magma body, and we suggest these factors may explain why this pattern is relatively rare.

1 Introduction

Long-lived active volcanic centers are the uppermost expression of a complex transcrustal transport system bringing magma from beneath and within the lithosphere to the surface (e.g., Hildreth & Wilson, 2007; Cashman et al., 2017). These systems comprise partially molten regions throughout the crust, thought to be a combination of crystal poor magma bodies surrounded by crystal rich "mush" zones near solidus (Cooper & Kent, 2014; Glazner et al., 2016; Jackson et al., 2018). Mush zones, where crystal volume fractions exceed 50-60%, are thought to be deformable but not readily eruptible (e.g., A. Costa et al., 2009; Bachmann & Bergantz, 2008). Within them, the formation of crystal-poor ($< 50\%$ crystals by volume) eruptible magma (e.g., Hughes et al., 2021) by heat and mass transfer is the subject of multidisciplinary exploration (e.g., F. Costa et al., 2020; Bergantz et al., 2015). Magma-mush interactions have been modeled as (visco)poroelastic coupling over length scales of magma intrusions (Mullet & Segall, 2022; Liao et al., 2018, 2021; Alshembari et al., 2023), or permeable flow and transport (Liu & Lee, 2021), possibly including the effects of volatiles (e.g., Parmigiani et al., 2014).

Mush zones in the upper crust are well documented at a number of active volcanic centers (e.g., Hamling et al., 2015), however, the role of mush in the mid-/lower crust is less well understood (Annen et al., 2006; Maguire et al., 2022; Magee et al., 2018). For example, seismic observations at two large and dynamic mid-crustal magma bodies, the Socorro Magma Body (SMB) and the Altiplano-Puna Magma Body (APMB), suggest the a broad (>100 km wide; e.g., Fig. 1a) region of anomalously low seismic wavespeeds in the mid-crust (Ward et al., 2014; Pritchard & Gregg, 2016; Gao et al., 2004; West et al., 2004; Wilson et al., 2005). These seismic anomalies coincide with volcanism (e.g., at the APMB, Long Valley, or Yellowstone) or elevated surface heatflow (e.g., Reiter et al., 2010), anomalous resistivity structure (e.g., Comeau et al., 2015), and the presence of anomalous seismicity (Sanford et al., 2002; Jay et al., 2012; Hudson et al., 2022; Rinehart & Sanford, 1981; Stankova et al., 2008), suggesting they are thermally/mechanically anomalous. While these regional mid-crustal seismic anomalies are consistent with the presence of melt (Maguire et al., 2022; Magee et al., 2018; Ake & Sanford, 1988), we lack an understanding of how magma and mush may be distributed within them and what role they play in the larger transcrustal magma transport system. For example, the APMB underlies numerous volcanoes (Magee et al., 2018; Gottsmann et al., 2017) and it is not clear how magma and mush are distributed within it. Thermal modeling of episodic melt injection suggests prolonged heating is necessary to generate long-lived mush zones (Annen et al., 2015; Blundy & Annen, 2016; Karakas et al., 2017). Such mush zones are likely weaker than the surrounding crust (Diener & Fagereng, 2014), but the implications of the resulting rheologic heterogeneity have not been fully considered in studies of surface deformation due to pressurizing mid-crustal magma bodies.

Inspired by regionally-extensive mid-crustal seismic anomalies, we use numerical models to study the role of spatial (horizontal and vertical) heterogeneity within the mid-crust in controlling the surface deformation response to mid-crustal magma pressurization. We are interested in the mechanical coupling between a mid-crustal compliant region (CR) and a pressurizing sill-like magma body. Separating surface deformation patterns due to mid-crustal magma injection and shallower magma dynamics proves difficult where the magma transport system extends to a volcanic system (e.g., Uturuncu Volcano, Long Valley, or Yellowstone) as upper crustal deformation obscures deeper processes (Biggs & Pritchard, 2017). We therefore focus on the SMB (Fig. 1), a large, seismically inferred, sill-like magma body at 19 km depth (diameter 50−70 km and thickness < 1 km; Rinehart & Sanford, 1981; Balch et al., 1997; Fialko et al., 2001), which does not have a volcanic expression.

Our starting point is a pattern of central uplift surrounded by subsidence, so-called "sombrero uplift" (coined by Fialko & Pearse, 2012), observed above both the SMB (Larsen et al., 1986; Pearse & Fialko, 2010; Fialko & Pearse, 2012; Finnegan & Pritchard, 2009) and the APMB at Uturuncu volcano (Fialko & Pearse, 2012; Henderson & Pritchard, 2017; Gottsmann et al., 2018). For the APMB this deformation has been modeled as deformation that couples magma injection at depth with either deeper crustal mechanics (Fialko & Pearse, 2012; Henderson & Pritchard, 2017), or the dynamics of a shallow upper-crustal mush zone (Gottsmann et al., 2017). The SMB, however, lacks an upper crustal expression of the magma transport system motivating the question of how such a sombrero pattern might arise and what impact the presence of a CR may have.

A key finding of our study is that a mid-crustal CR surrounding the SMB leads to a spatial decoupling of surface deformation. Generally, vertical surface uplift directly above a pressurizing sill-like body (radius r_{source}) within a CR may be accompanied by surface subsidence of regions toward the edges of the CR ($r \gtrapprox 1.5 r_{source}$), providing an alternative mechanism for emergence of the sombrero pattern. The transient nature of the somberro pattern and its duration ($\Delta\tau_{som}$) is a strong function of the rheologic gradients within the CR and the pressure-time history within the sill, providing an explanation for its rare observation. Importantly, the surface expression of the deformation is controlled by the interplay of the pressurization timescale and the effective (viscoelastic) response timescale in the CR.

2 Deformation observations at the Socorro Magma Body

At the SMB, the sombrero pattern of surface motion has been measured over nearly 100 years through leveling (Larsen et al., 1986) and Interferometric Synthetic Aperture Radar (InSAR) (Fialko et al., 2001; Pearse & Fialko, 2010). These observations, together with other geodetic measurements (Berglund et al., 2012; Larsen et al., 1986), suggest a maximum vertical uplift rate of $\approx 2 - 2.5$ mm/yr.

We acquire Synthetic Aperture Radar (SAR) observations on ascending path 49 frame 107 (Fig. 1b), collected by the European Space Agency's Sentinel-1 A/B mission (Torres et al., 2012), which we process with GMTSAR (Sandwell et al., 2011) to create 2 pass interferograms spanning January 2017 though December 2021. We create mean velocity stacks (supplementary text S1) from individual interferograms which include December through January multi-year pairs by averaging the observed line-of-sight (LOS) deformation over the time interval of acquisition where observations are weighed by the time interval (e.g., Xiao et al., 2020). The resulting LOS velocity field (Fig. 1b), aligned with prior observations (Pearse & Fialko, 2010; Finnegan & Pritchard, 2009; Fialko et al., 2001) to fit the magnitude of observations, reveals deformation overlying the SMB. From the average LOS deformation map (Fig. 1b), we extract profiles for comparison to our SMB-specific finite-element model results (Fig 5c). We observe $\approx$ 3 mm/yr of peak LOS uplift within the SMB, with uplift limited to the central to western portion of the magma body. North-south and east-west profiles across the peak deformation illustrate the sombrero uplift over the magma body as described by Pearse and Fialko (2010). While residual topography impacts may bias the velocity field, we do not observe similar effects over other nearby topography.

Previous InSAR observations over the SMB report deformation rates of 2-3 mm/yr (Pearse & Fialko, 2010; Finnegan & Pritchard, 2009; Fialko et al., 2001), comparable to our observations during the duration of the SAR acquisitions. We observe a north-south elongated region of uplift, more consistent with Fialko et al. (2001) than the circular deformation shown by Finnegan and Pritchard (2009). Temporal changes in the InSAR-derived average LOS velocities over the SMB were presented in Finnegan and Pritchard (2009), therefore, variations in the shape of the region experiencing uplift during our study are not unprecedented.

This deformation signal is generally attributed to injection of magma in the mid-crust, however, many studies suggest it cannot be due to solely elastic effects (e.g., Fialko et al., 2001; Pearse & Fialko, 2010; Fialko & Pearse, 2012). Previous models of deformation at the SMB (Larsen et al., 1986; Fialko et al., 2001; Pearse & Fialko, 2010; Finnegan & Pritchard, 2009; A. Newman et al., 2001; A. V. Newman et al., 2006) do not explicitly consider material heterogeneity in a mid-crustal CR, the main target of our investigation.

3 Numerical Modeling Results

We present generic finite element models using PyLith (v2.2.2; Aagaard et al., 2017), to assess the role of a CR surrounding a sill-like pressure source in the mid-crust. We target the role of the CR and its manifestation in ground deformation (parameters and model details in supplementary text S2, Table S1, and Fig. S1). Each model comprises a background layered structure, with deformation driven by time-varying pressurization of a mid-crustal sill (Fig. 2b). We consider a suite of models, with and without a viscoelastic CR surrounding the sill, and explore the effects of varying CR structure (Fig. 2a; Table S1).

A viscoelastic CR in the mid-crust (with lower viscosity than the ambient viscoelastic crust), leads to a phase-lag in surface deformation. When the sill within the CR undergoes pressurization, regions above its center and those to its edges (e.g., $r \geq 1.5r_{source}$) may be out of phase (demonstrated for vertical motions in Fig 3a and for horizontal motions in Fig S3). This is the essence of the sombrero signal (central uplift surrounded by an annular moat of subsidence), and we observe this pattern during the (re-)pressurization phase (Fig. 2b), where the center begins to uplift while the edges are still subsiding due to viscoelastic relaxation of the CR. The sombrero pattern is only observed in the presence of a CR (Fig. 3a); without it, surface velocities are in phase everywhere and have the same sign (Fig 3b).

When a CR exists, surface motions above the source (within $r/r_{source} \leq 1$) and outside it ($r/r_{source} \gtrapprox 1.5$) depend on: (1) rheologic gradients within the CR and (2) the applied pressurization history (Fig. 3c-f). Depending on the gradient of viscosity within the CR, we observe a circulatory pattern of motion in the mid-crust (e.g., Fig. 2d,e) and a phase lag between vertical surface velocities above the sill ("center") and outside of the source radius ("shoulder"; Fig. 3c-f; see also Fig S2). The time interval when vertical velocities at the center are positive and the shoulder regions are subsiding is the sombrero duration, $\Delta\tau_{som}$ (and vice versa, for a "reverse" sombrero, e.g., Fig 3d).

Spatial decoupling of the center and shoulder velocities during sombrero deformation depends on the rheologic gradient within the CR: comparing uniform CR model vs models with horizontal ("nested") and vertical ("stacked") viscosity gradients (Fig. 2a). A larger CR viscosity gradient increases the phase lag compared to the uniform CR models (Fig. S2b, d), with systematically higher phase lags in the nested CR model than the stacked CR model (Fig. S2). Horizontal viscosity gradients are, therefore, more important than vertical ones for controlling sombrero-style deformation.

In addition to rheologic gradients, the phase lag in surface velocities is strongly controlled by the pressure-time function. Sinusoidal pressure-time functions yield periodic motions where $\Delta\tau_{som}$ corresponds to a fixed (phase- and) time-lag for both the sombrero and the reverse sombrero (Fig. 3c,d,f). For sawtooth pressurization, however, the duration of the sombrero may greatly exceed that of the reverse pattern (Fig. 3e). Nested CR models driven by sawtooth pressurization (Fig. 3e) exhibit near-constant surface velocities during a sombrero event.

Decreasing the pressurization rate (e.g., $dP/dt \approx 4\Delta P/T$ for the sinusoidal function) leads to increased sombrero duration, $\Delta\tau_{som}$ (Fig. 4). The sombrero duration $\Delta\tau_{som}$ for a given $\Delta P/T$ increases with the ambient background pressure, P_0, and decreases with relaxation time t_r (Fig 4a). For the uniform CR, the relation between $\Delta\tau_{som}$ and $\Delta P/T$ collapses into a single trend when the duration is normalized by the uniform relaxation time within the CR, t_r, and the pressurization rate is normalized by P_0/t_r (Fig. 4b). Nested and stacked CR runs also collapse onto similar trends showing an increase in $\Delta\tau_{som}$ at low $\Delta P t_r/P_0 T$, with systematically higher sombrero durations compared to the uniform CR models at the same dimensionless pressurization rate (Fig. 4b). (We use a volumetrically-averaged relaxation time to nondimensionalize in non-uniform CRs). For the uniform and stacked CR models, there is a transition at low $\Delta P t_r / P_0 T$ at which the sombrero duration is not as sensitive to the pressurization rate. The slope of the trend is similar for nested CR models, but without a similar observed transition at low rates. (Reaching a dimensionless pressurization rate of $\Delta P t_r / P_0 T = 10^{-2}$ is computationally expensive for the nested and stacked CR models due to the large volumetrically-averaged t_r.) The uniform and stacked CR models clearly reach a threshold at which $\Delta \tau_{som}$ appears to be nearly independent of $\Delta P t_r / P_0 T$, suggesting the threshold depends on intra-CR rheology ($\Delta P t_r / P_0 T \approx 10^{-2}$ for uniform CR and 10^{-1} for stacked CR; Fig. 4b). Models with the same pressurization rate but different pressure-time functions show little variation in sombrero duration, demonstrating that the primary controlling factors for sombrero duration are the pressurization rate and model geometry, and not pressure-time history (Fig. 4).

4 Discussion

While idealized, the generic models above demonstrate that a weaker-than-ambient CR surrounding a (de-)pressurizing sill can decouple surface deformation directly above the sill from deformation laterally displaced from the sill. A key finding is that, during pressurization, locations vertically above the sill may be uplifting while those outside the surface projection of the sill may be subsiding, creating a sombrero pattern (Fig. 3). (The pattern may be reversed when transitioning to a period of de-pressurization.) This phase lag in the surface deformation pattern depends on the presence of the CR, but the duration of the sombrero depends primarily on pressurization rate: increasing with decreasing pressurization rate, up to a threshold (Fig. 4). Strong viscosity gradients paired with asymmetric pressurization lead to long sombrero durations with nearly steady ground motions (Fig. 3e and Fig. 4b). Crucially, a long period of re-pressurization (with roughly constant dP/dt) followed by a sudden decrease in pressure results in a sombrero that lasts longer than the reverse-sombrero, with slowly-varying surface velocities during the sombrero (Fig. 3d). Although we lack contraints on SMB sill pressures, rheologic properties of anatexites suggest that the the bulk strength of partially-molten rocks in the mid-/lower crust range from $\leq 1 - 5$ MPa during cycles of melt production and drainage (Diener & Fagereng, 2014). The range of background pressures, P_0, and pressure changes ΔP, in our models (Fig. 4) is consistent with expectations for weakened partially molten crustal mineralogies (Diener & Fagereng, 2014).

We now present an SMB-specific model constrained by seismic and geodetic observations discussed above: (1) a sill-like body at $\approx$ 19 km depth, elliptical in mapview, surrounded by anomalously low V_s in the mid-crust (Balch et al., 1997; Rinehart & Sanford, 1981; West et al., 2004, ; Fig 1a); and (2) a long-lived ($\Delta\tau_{som} \geq$ 100 yrs) sombrero pattern of deformation, with nearly constant surface motions (Fialko et al., 2001; Pearse & Fialko, 2010; Finnegan & Pritchard, 2009; Larsen et al., 1986, Fig. 1). Assuming that the $V_s \leq 5\%$ at $\approx$ 20 km depth region in West et al. (2004) is a proxy for a weaker-than-ambient CR (dashed yellow circle in Fig 1b), we specify horizontal and vertical gradients in CR viscosity (see Table S1). The 200 km diameter of the hybrid CR follows the extent of the low-velocity mid-crustal V_s anomaly and the sill-like ellipsoidal source has thickness 1 km and mapview radii of 24 and 38 km (Fig 5a). With this geophysically-informed SMB-model, we explore the background pressure P_0 needed to match the amplitude of the InSAR LOS observations and the pressurization rate dP/dt needed to generate a long-lived (> 100 yr) sombrero pattern.

We find that a sill pressurized to a background pressure of P_0=1.0 MPa, with a constant pressure increase of $dP/dt = 4\Delta P/T = 5$ kPa/yr (implemented as a sawtooth pressure-time function with ΔP=250 kPa and $T = 200$ yrs; Fig 5b), produces a reasonable fit to the InSAR observations (A-A' and B-B' in Fig. 5c). The modeled sombrero duration of $\Delta\tau_{som} = 148$ yrs is characterized by persistent, nearly steady surface motions for over 100 yrs, comparable to long-term observations at the SMB (Fig.5c). The width of the modeled deformation depends on the seismically-constrained geometry, and no further adjustment was used to fit the width of the surface pattern in Fig. 5c.

The inferred pressurization rate of $dP/dt \approx 5$ kPa/yr (comparable to Pearse & Fialko, 2010) may be interpreted as due to injection of magma, or to pressurization due to volatile degassing. If driven by magma injection, we infer a volumetric rate $dV/dt = \beta V_0(dP/dt)$ where β is the magma compressibility and V_0 is an initial volume. Compressibility of a gas-poor, basaltic magma at 19 km depth is likely lower than compressibility above 10 km depth (e.g., $\beta \approx 0.4 - 2 \times 10^{-10}$ Pa^{-1}; Rivalta and Segall (2008)), so $\beta = 0.4 \times 10^{-10}$ Pa^{-1} is a reasonable upper bound. Following pressurization to $P_0 \approx$ 1 MPa, the initial volume of the ellipsoidal source (Table S1) is ≈ 1940 km^3, so $dV/dt \approx 3.88 \times 10^{-4}$ km^3/yr. If the source includes exsolved volatiles, the inferred volumetric injection rate is likely too large. A dry (≤ 0.2 wt % H_2O) basaltic magma (e.g., expected in a rift-setting) with ≥ 4000 ppm CO_2 at ≥ 1000°C is likely to reach saturation at pressures above 500 MPa, comparable to conditions at 19 km depth within the Rio Grande Rift. We lack direct constraints on the CO_2 content of the SMB, however, mantle xenoliths from the nearby Rio Puerco and Kilbourne Hole Volcanic Fields have undergone metasomatism by carbonatitic fluids (Porreca & Selverstone, 2006; Harvey et al., 2012), suggesting that pressurization may be a signal of gas exsolution rather than magma injection.

Observations at the APMB span a shorter timeframe than the SMB, and suggest a peak uplift rate at Uturuncu Volcano of $\approx 0.5-1$ cm/yr (Fialko & Pearse, 2012; Henderson & Pritchard, 2017; Gottsmann et al., 2018). Here, 50 years of geodetic observations suggest transient sombrero deformation (Fialko & Pearse, 2012; Eiden et al., 2023; Gottsmann et al., 2018), and our models provide an explanation for this transience. The inferred pressurization rate at the SMB (≈ 5 kPa/yr) is smaller than modeled beneath Uturuncu if all of the deformation is ascribed to upper crustal processes (Gottsmann et al., 2017). As we have demonstrated, for a given pressurization rate the duration of the sombrero pattern is controlled by decoupling between surface motions within $r < 1.5r_{source}$ and $r \geq 1.5r_{source}$, and this decoupling and phase lag depends on intra-CR viscosity gradients (Fig S2). Specifically, sombrero durations will be smaller (and therefore manifest their transience over shorter timescales) if the mid-crustal CR is uniform in rheology vs. if it has significant rheologic gradients within it (Figs 4; S2). Our models raise the possibility that at least part of the transient sombrero pattern in the APMB may indeed be attributed to lateral heterogeneity in the mid-crust, with perhaps a more rheologically uniform CR than in the SMB.

While these results make a compelling case for mid-crustal magmatic processes in controlling the SMB geodetic signal, we acknowledge important complexities are ignored in our models, e.g., near-surface hydrology and groundwater extraction (likely evident at the southern end of profile B-B' in Fig 5c, which crosses from the Socorro Basin into the Jornada del Muerto Basin). We also ignore extensional stress and material heterogeneity associated with the Rio Grande Rift. In future work, we hope to include heat transfer and poro(visco)-elastic effects to more fully explore CR heterogeneity and implications for magma-mush interactions. During time-variable pressurization in the sill, as magma is either sourced from deeper levels or drained from a mush, we might expect time-dependent rheology in the CR as explored in Liao et al. (2021, 2018); Mullet and Segall (2022); Alshembari et al. (2023). These studies explore interactions in a single melt injection/withdrawal event, however, our models highlight the importance of cyclic pressure-time variations, especially when a CR is present, in decoupled surface deformation. As shown by Liao et al. (2021), two important time scales for controlling stress transfer and surface deformation include a short time scale driven by poroelastic diffusion, and a longer viscoelastic relaxation time scale. Indeed, the fast depressurization in the sawtooth function may be a proxy for porous diffusion of magma into the surrounding CR mush zone, causing depressurization at a significantly faster rate than allowed by viscous relaxation. Over longer timescales, however, poroviscoelastic effects may be less important than the viscous relaxation behavior captured in our models. Specifically, viscous creep within a weaker-than-ambient mid-crustal CR (e.g., a regionally-extensive partial melt-rich mush) and intra-CR rheologic gradients drive transient surface deformations as seen in the sombrero pattern.

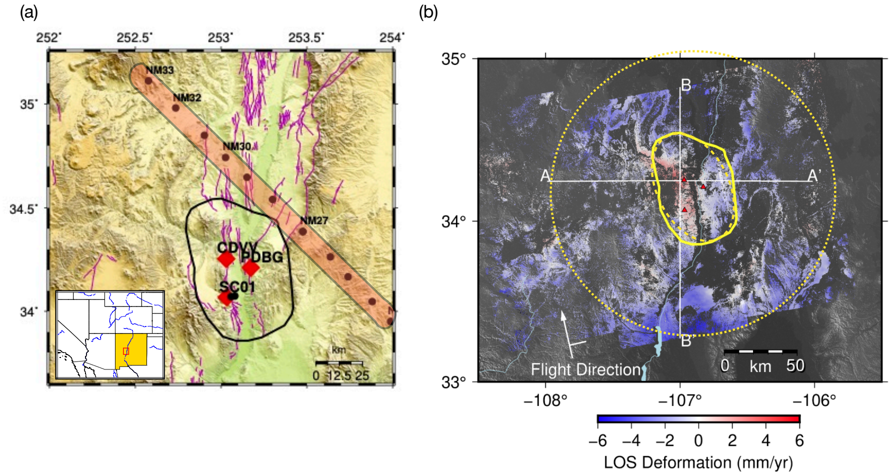

Figure 1. a) Topographic relief map of the seismically derived extent of the Socorro Magma Body (SMB), New Mexico, (Rinehart & Sanford, 1981; Balch et al., 1997), within southwestern North America (inset). Quaternary faults (magenta lines), three continuous GPS stations (red diamonds), and locations of the La Ristra seismic stations (black dots) (West et al., 2004) indicated for reference. The orange polygon outlines the NW-SE extent of low mid-crustal seismic wavespeeds ($\Delta V_s < 5\%$ at ≈ 20 km depth, from (West et al., 2004). (b). InSAR measurements of the SMB spanning 01/07/2017 through 12/21/2021 showing the observed sombrero-style surface deformation. GPS stations (red) and the SMB outline (solid yellow) are as in (a). The yellow ellipse (long-dashes) outlines the pressure source and the larger yellow circle (short-dashes) shows the map-extent of the CR in the SMB-realistic model (Fig. 5).

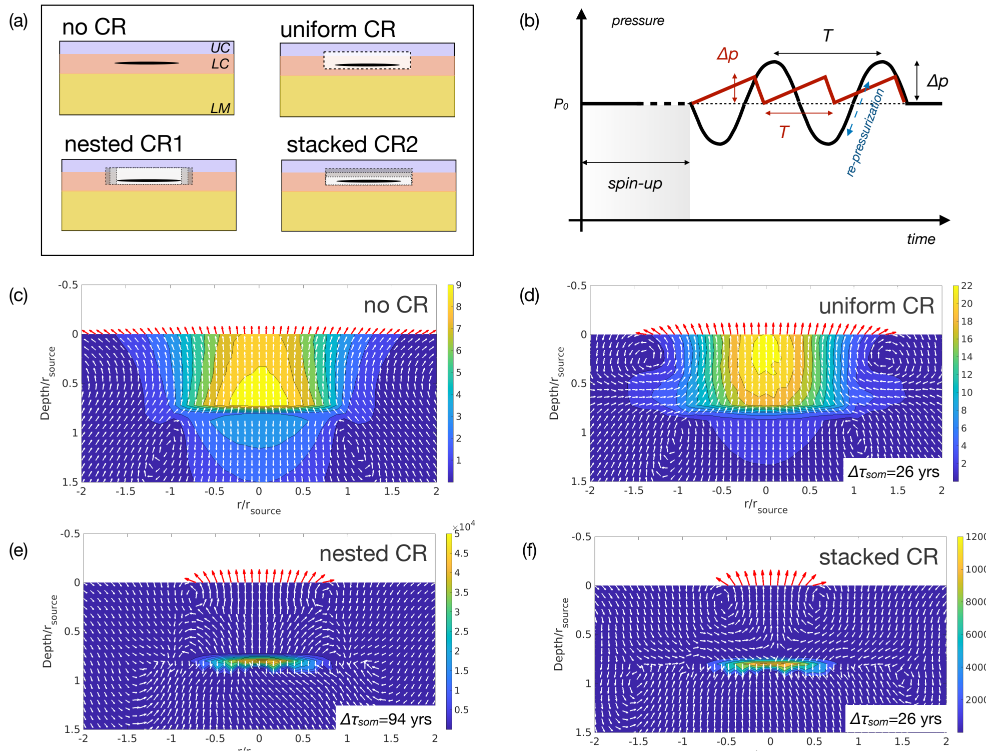

Figure 2. (a) Cross-section cartoons of generic models with variable CR. All models share a layered background rheology (UC=upper crust, LC=lower crust, LM=lithospheric mantle; see S2), within which a mid-crustal pressure source is embedded (black ellipse). The CR rheology is specified with a single viscosity (uniform CR) or with horizontal gradient in nested cylinders (nested CR) or vertical gradient in stacked cylinders (stacked CR). The nested CR viscosity increases radially and the stacked CR has viscosity increasing vertically. (b) After initial pressurization to a background pressure P_0, followed by a prescribed "spin-up" time at constant pressure, one of two periodic pressure functions is applied: a sinusoid with amplitude ΔP and period T (black), or sawtooth with pressure change ΔP and period T (red). The "re-pressurization" phase of a given pressure-time function refers to intervals with $dP/dt > 0$ as indicated (blue dashed arrows). (c)-(f) Cross sections illustrating spatially-varying velocity (arrows) for models with the same $r_{source} = 25$ km, P_0=1 MPa, ΔP=500 kPa and T=200 yrs, (with sinusoidal pressurization), but with differing CR: (c) no CR, (d) a uniform CR, (e) nested CR, and (f) stacked CR. Velocity snapshots are shown halfway during the sombrero (d-f; durations indicated) or halfway through a pressure cycle (c). Red arrows show upward surface motions and color contours indicate velocity magnitude (mm/yr).

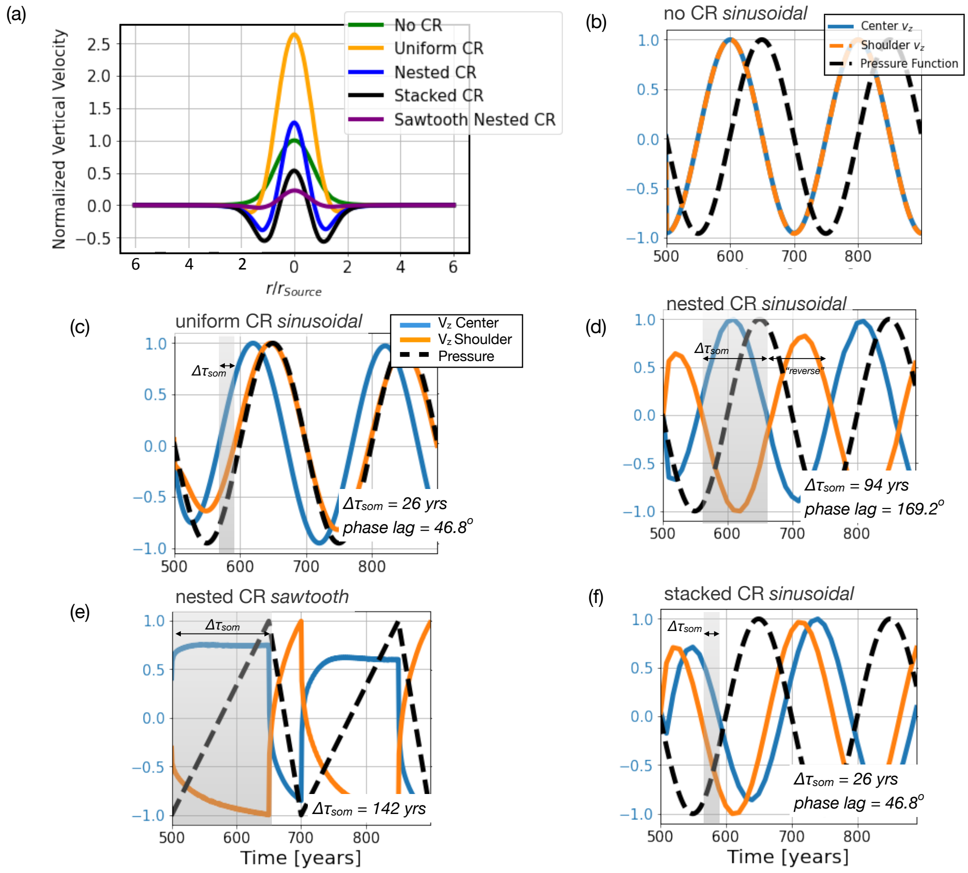

Figure 3. (a) Normalized vertical surface velocity, V_z, profiles (normalized relative to the maximum velocity of the no CR case), illustrating the role of the CR in the sombrero pattern of deformation in four models with varying CR; all with P_0=1MPa, ΔP=500kPa and T=200yrs. Each profile is shown at the same times as the corresponding velocity fields in Fig. 2c-f; see Fig S3 for corresponding radial motions. (b)-(d): Normalized surface uplift velocities at the center (r = 0 km, blue) and shoulder (defined as r/r_{source} = 1.6, orange), with normalized sinusoidal pressure-time variation (black dashed lines): (b) no CR (corresponds to model in Fig. 2c), (c) a uniform CR (model in Fig. 2d), and (d) nested CR (model in Fig. 2e). (e)-(f) show decoupled center and shoulder velocities for the (e) nested CR and (f) stacked CR driven by pressurization functions as indicated.

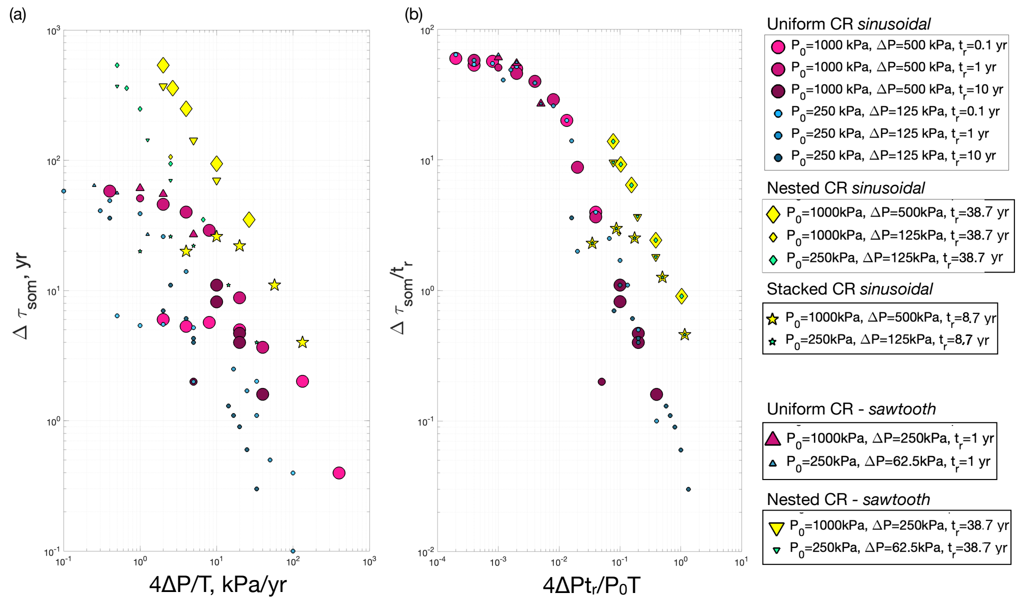

Figure 4. (a) Sombrero duration as a function of pressurization rate for the suite of models in this study. (b) Dimensionless sombrero duration (normalized by CR relaxation time) vs dimensionless pressurization rate (normalized by background pressure and CR relaxation time). In (a) and (b), we see a general trend of increasing sombrero duration with decreasing pressurization rate, up to a threshold. Nondimensionalization collapses all uniform CR runs into a single trend, and likewise with the nested CR and stacked CR models. To normalize nested CR and stacked CR runs, t_r was found by volumetrically averaging the relaxation times within the CR.

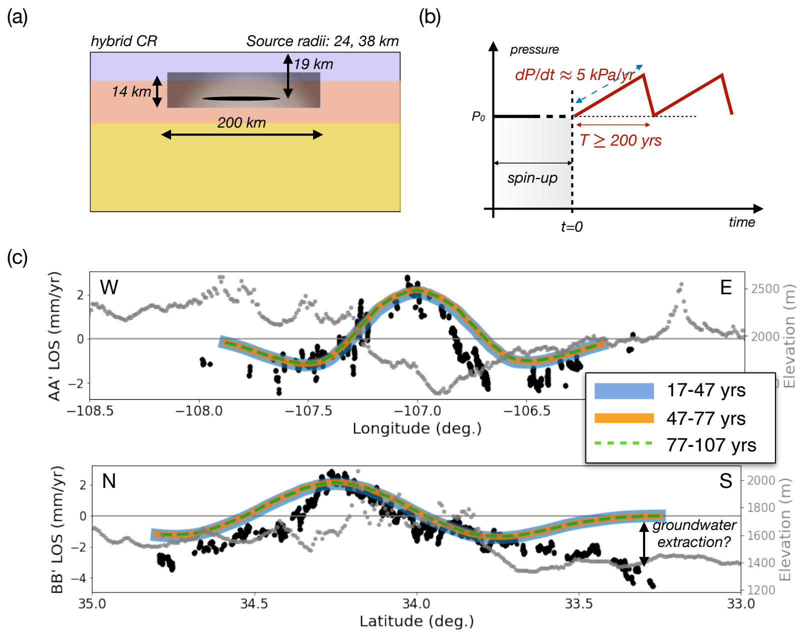

Figure 5. Summary of SMB-realistic ellipsoidal source/hybrid CR model (Table S1) and results. (a) Cartoon schematic illustrating the CR (200 km diameter), with both horizontal and vertical gradients in t_r (represented by the shading moving away from the pressure source (black); Table S1). (b) Sketch of pressure-time function, with constant pressurization at $dP/dt \approx 5$ kPa/yr, leading to a nearly stationary sombrero pattern over $\Delta t_{som} > 100$ yrs (sawtooth period $T \geq 200$ yrs). (c) Predicted surface velocity profiles (solid and dashed lines) extracted along lines A-A' and B-B' in Fig 1b, projected onto the LOS and averaged over 30 yr windows as indicated (t=0 is defined at the beginning of the sawtooth function in (b)). Lines extracted from the model are offset by 10.0 km west and 0.5 km north and rotated by -22.55°. InSAR LOS velocities along profiles A-A' and B-B' (black dots) and topography (light gray dots) are plotted for comparison. The misfit at the southern end of the B-B' profile is likely due to groundwater extraction from local agricultural activity.

5 Open Research

All PyLith input files will be made available at the following github repository: https://github.com/Grant-Block/SMB_FiniteElementModels

The PyLith software is freely available at: https://github.com/geodynamics/pylith

Acknowledgments

GB and MR thank: the UNM Center for Advanced Research Computing, supported in part by the National Science Foundation, for resources used in this work; Eric Lindsey for fruitful InSAR discussions; and David Wilson and Mike West for information regarding the La Ristra seismic experiment. MR thanks Emmanuel Codillo for discussions on the magma saturation pressures during the CIDER 2023 workshop. GB also thanks the CONVERSE network for discussions which helped inform and contextualize this project. EG and RG acknowledge NASA funding through ŁNIP #80NSSC20K0073. Copernicus Sentinel data 2016-2020. Retrieved from ASF DAAC, processed by ESA.

References

Aagaard, B., Knepley, M., & Williams, C. (2017). *Pylith v2.2.2 [software].* Davis, CA. doi: http://doi.org/10.5281/zenodo.438705

Ake, J., & Sanford, A. (1988). New evidence for the existence and internal structure of a thin layer of magma at mid-crustal depths near socorro, new mexico. *Bulletin of the Seismological Society of America*, *78*, 1335–1359. doi: 10.1785/BSSA0780031335

Alshembari, R., Hickey, J., Williamson, B. J., & Cashman, K. (2023). Unveiling the rheological control of magmatic systems on volcano deformation: The interplay of poroviscoelastic magma-mush and thermo-viscoelastic crust. *Journal of Geophysical Research: Solid Earth*, *128*(7), e2023JB026625. Retrieved from `https://agupubs.onlinelibrary.wiley.com/doi/abs/10.1029/2023JB026625` (e2023JB026625 2023JB026625) doi: https://doi.org/10.1029/2023JB026625

Annen, C., Blundy, J. D., Leuthold, J., & Sparks, R. S. J. (2015). Construction and evolution of igneous bodies: Towards an integrated perspective of crustal magmatism. *Lithos*, *230*, 206–221. doi: https://doi.org/10.1016/j.lithos.2015.05.008

Annen, C., Blundy, J. D., & Sparks, R. S. J. (2006). The genesis of intermediate and silicic magmas in deep crustal hot zones. *Journal of Petrology*, *47*, 505–539. doi: 10.1093/petrology/egi084

Bachmann, O., & Bergantz, G. (2008). The magma reservoirs that feed supereruptions. *Elements*, *4*, 17-21. doi: 10.2113/GSELEMENTS.4.1.17

Balch, R. S., Hartse, H. E., Sanford, A. R., & wan Lin, K. (1997). A new map of the geographic extent of the socorro mid-crustal magma body. *Bulletin of the Seismological Society of America*, *87*(1), 174-182.

Bergantz, G. W., Schleicher, J. M., & Burgisser, A. (2015). Open-system dynamics and mixing in magma mushes. *Nature Geoscience*, *8*, 793–796. doi: 10.1038/ngeo2534

Berglund, H. T., Sheehan, A. F., Murray, M. H., Roy, M., Lowry, A. R., Nerem, R. S., & Blume, F. (2012). Distributed deformation across the rio grande rift, great plains, and colorado plateau. *Geology*, *40*(1), 23-26. doi: 10.1130/G32418.1

Biggs, J., & Pritchard, M. E. (2017, 02). Global Volcano Monitoring: What Does It Mean When Volcanoes Deform? *Elements*, *13*(1), 17-22. Retrieved from `https://doi.org/10.2113/gselements.13.1.17` doi: 10.2113/gselements.13.1.17

Blundy, J. D., & Annen, C. J. (2016). Crustal magmatic systems from the perspective of heat transfer. *Elements*, *12*(2), 115–120. doi: https://doi.org/10.2113/gselements.12.2.115

Cashman, K. V., Sparks, R. S. J., & Blundy, J. D. (2017). Vertically extensive and unstable magmatic systems: A unified view of igneous processes. *Science*, *355*, 1280. doi: 10.1126/science.aag3055

Comeau, M. J., Unsworth, M. J., Ticona, F., & Sunagua, M. (2015). Magnetotelluric images of magma distribution beneath volcan uturuncu, bolivia: Implications for magma dynamics. *Geology*, *34*(243-246). doi: 10.1130/G36258.1

Cooper, K. M., & Kent, A. J. R. (2014). Rapid remobilization of magmatic crystals kept in cold storage. *Nature*, *506*(480-483). doi: 10.1038/nature12991

Costa, A., Caricchi, L., & Bagdassarov, N. (2009). A model for the rheology of particle-bearing suspensions and partially molten. *Geochemistry Geophysics Geosystems*, *10*(Q03010). doi: 10.1029/2008GC002138

Costa, F., Shea, T., & Ubide, T. (2020). Diffusion chronometry and the timescales of magmatic processes. *Nature Reviews Earth and Environment*. Retrieved from `https://doi.org/10.1038/s43017-020-0038-x` doi: 10.1038/s43017-020-0038-x

Diener, J. F. A., & Fagereng, Å. (2014). The influence of melting and melt drainage on crustal rheology during orogenesis. *Journal of Geophysical Research, Solid Earth*, *119*, 6193–6210. doi: 10.1002/2014JB011088

Eiden, E., MacQueen, P., Henderson, S., & Pritchard, M. E. (2023). Multiple spatial and temporal scales of deformation from geodetic monitoring point to active transcrustal magma system at uturuncu volcano, bolivia. *Geosphere*, *19*(X), 1-13. doi: 10.1130/GES02520.1

Fialko, Y., & Pearse, J. (2012). Sombrero uplift above the altiplano-puna magma body: Evidence of a ballooning mid-crustal diapir. *Science*, *338*(6104), 250–252. doi: 10.1126/science.1226358

Fialko, Y., Simons, M., & Khazan, Y. (2001). Finite source modelling of magmatic unrest in socorro, new mexico, and long valley, california. *Geophysical Journal International*, *146*(1), 191–200. doi: 10.1046/j.1365-246X.2001.00453.x

Finnegan, N., & Pritchard, M. (2009). Magnitude and duration of surface uplift above the socorro magma body. *Geology*, *37*(3), 231-234. Retrieved from `https://doi.org/10.1130/G25132A.1` doi: 10.1130/G25132A.1

Gao, W., Grand, S., Baldridge, W. S., Wilson, D., West, M., Ni, J., & Aster, R. (2004). Upper mantle convection beneath the central Rio Grande rift imaged by P and S wave tomography. *Journal of Geophysical Research*, *109*. doi: 10.1029/2003JB002743

Glazner, A., Bartley, J., & Coleman, D. (2016). We need a new definition for "magma". *EOS*, *97*. doi: 10.1029/2016EO059741

Gottsmann, J., Blundy, J., Henderson, S., Pritchard, M., & Sparks, R. (2017). Thermomechanical modeling of the altiplano-puna deformation anomaly: Multiparameter insights into magma mush reorganization. *Geosphere*, *13*(4), 1-24. doi: 10.1130/GES01420.1

Gottsmann, J., delPotro, R., & Muller, C. (2018). 50 years of steady ground deformation in the altiplano-puna region of southern bolivia. *Geosphere*, *14*(1), 65-73. doi: 10.1130/GES01570.1.

Hamling, I. J., Hreinsdottir, S., & Fournier, N. (2015). The ups and downs of the tvz: geodetic observations of deformation around the taupo volcanic zone, new zealand. *Journal of Geophysical Research: Solid Earth*, *120*, 4667–4679. doi: 10.1002/2015JB012125.

Harvey, J., Yoshikawa, M., Hammond, S. J., & Burton, K. W. (2012). Deciphering the trace element characteristics in kilbourne hole peridotite xenoliths: Melt-rock interaction and metasomatism beneath the rio grande rift, sw usa. *Journal of Petrology*, *53*(8), 1709-1742.

Henderson, S. T., & Pritchard, M. E. (2017, 10). Time-dependent deformation of Uturuncu volcano, Bolivia, constrained by GPS and InSAR measurements and implications for source models. *Geosphere*, *13*(6), 1834-1854. doi: 10.1130/GES01203.1

Hildreth, W., & Wilson, C. J. N. (2007). Compositional zoning of the bishop tuff. *Journal of Petrology*, *48*(5). doi: 10.1093/petrology/egm007

Hudson, T. S., Kendall, J.-M., Pritchard, M. E., Blundy, J. D., & Gottsmann, J. H. (2022). From slab to surface: Earthquake evidence for fluid migration at uturuncu volcano, bolivia. *Earth and Planetary Science Letters*, *577*. Retrieved from `https://doi.org/10.1016/j.epsl.2021.117268` doi: 10.1016/j.epsl.2021.117268

Hughes, G. E., Petrone, C. M., Downes, H., Varley, N. R., & Hammond, S. J. (2021). Mush remobilisation and mafic recharge: A study of the crystal cargo of the 2013–17 eruption at volcán de colima, mexico. *Journal of Volcanology and Geothermal Research*, *416*. doi: 10.1016/j.jvolgeores.2021.107296

Jackson, M. D., Blundy, J., & Sparks, R. S. J. (2018). Chemical differentiation, cold storage and remobilization of magma in the earth's crust. *Nature*, *564*, 405-409. doi: 10.1038/s41586-018-0746-2

Jay, J. A., Pritchard, M. E., West, M. E., Christensen, D., Haney, M., Minaya, E., … Zabala, M.

Shallow seismicity, triggered seismicity, and ambient noise tomography at the long-dormant uturuncu volcano, bolivia. . doi: 10.1007/s00445-011-0568-7

Karakas, O., Degruyter, W., Bachmann, O., & Dufek, J. (2017, Jun 01). Lifetime and size of shallow magma bodies controlled by crustal-scale magmatism. *Nature Geoscience*, *10*(6), 446-450. Retrieved from `https://doi.org/10.1038/`

`ngeo2959` doi: 10.1038/ngeo2959

Larsen, S., Reilinger, R., & Brown, L. (1986). Evidence of ongoing crustal deformation related to magmatic activity near socorro, new mexico. *Journal of Geophysical Research: Solid Earth*, *91*(B6), 6283–6292. doi: 10.1029/JB091iB06p06283

Liao, Y., Soule, S. A., & Jones, M. (2018). On the mechanical effects of poroelastic crystal mush in classical magma chamber models. *Journal of Geophysical Research*, *123*(11). doi: 10.1029/2018JB015985

Liao, Y., Soule, S. A., Jones, M., & Le Mével, H. (2021). The mechanical response of a magma chamber with poroviscoelastic crystal mush. *Journal of Geophysical Research*, *126*(4). doi: 10.1029/2020JB019395

Liu, B., & Lee, C.-T. (2021). Fast melt expulsion from crystal-rich mushes via induced anisotropic permeability. *Earth and Planetary Science Letters*, *571*. Retrieved from `https://doi.org/10.1016/j.epsl.2021.117113` doi: 10.1016/j.epsl.2021.117113

Magee, C., Stevenson, C. T., Ebmeier, S. K., Keir, D., Hammond, J. O., Gottsmann, J. H., … Jackson, M. D. (2018). Magma plumbing systems: A geophysical perspective. *Journal of Petrology*, *59*(6), 1217–1251. doi: 10.1093/petrology/egy064

Maguire, R., Schmandt, B., Li, J., Jiang, C., Li, G., Wilgus, J., & Chen, M. (2022). Magma accumulation at depths of prior rhyolite storage beneath yellowstone caldera. *Science*, *378*, 1001–1004. doi: 10.1126/science.ade0347

Mullet, B., & Segall, P. (2022). The surface deformation signature of a transcrustal, crystal mush-dominant magma system. *Journal of Geophysical Research*, *127*. doi: 10.1029/2022JB024178

Newman, A., Dixon, T. H., Ofoegbu, G., & Dixon, J. E. (2001). Geodetic and seismic constraints on recent activity at long valley caldera, california: evidence for viscoelastic rheology. *Journal of Volcanology and Geothermal Research*, *105*(3), 183–206. doi: https://doi-org.libproxy.unm.edu/10.1016/S0377-0273(00)00255-9

Newman, A. V., Dixon, T. H., & Gourmelen, N. (2006). A four-dimensional viscoelastic deformation model for long valley caldera, california, between 1995 and 2000. *Journal of Volcanology and Geothermal Research*, *150*(1-3), 244–

269. doi: https://doi.org/10.1016/j.jvolgeores.2005.07.017

Parmigiani, A., Huber, C., & Bachmann, O. (2014). Mush microphysics and the reactivation of crystal-rich magma reservoirs. *Journal of Geophysical Research*, *119*, 6308–6322. doi: 10.1002/2014JB011124

Pearse, J., & Fialko, Y. (2010, 07). Mechanics of active magmatic intraplating in the rio grande rift near socorro, new mexico. *Journal of Geophysical Research*, *115*. doi: 10.1029/2009JB006592

Porreca, C., & Selverstone, J. (2006). Pyroxenite xenoliths from the rio puerco volcanic field, new mexico: Melt metasomatism at the margin of the rio grande rift. *Geosphere*, *2*(7), 333–351;.

Pritchard, M. E., & Gregg, P. M. (2016). Geophysical evidence for silicic crustal melt in the continents: Where, what kind, and how much? *Elements*, *12*(2), 121-127. doi: 10.2113/gselements.12.2.121

Reiter, M., Chamberlin, R. M., & Love, D. W. (2010). New data reflect on the thermal antiquity of the socorro magma body locale, rio grande rift, new mexico. *Lithosphere*, *2*(6), 447–453. doi: 10.1130/L115.1

Rinehart, E. J., & Sanford, A. R. (1981). Upper crustal structure of the rio grande rift near socorro, new mexico, from inversion of microearthquake s-wave reflections. *Bulletin of the Seismological Society of America*, *71*(2), 437–450. doi: https://doi.org/10.1785/BSSA0710020437

Rivalta, E., & Segall, P. (2008). Magma compressibility and the missing source for some dike intrusions. *Geophysical Research Letters*, *35*(4).

Sandwell, D., Mellors, R., Tong, X., Wei, M., & Wessel, P. (2011). Open radar interferometry software for mapping surface deformation. *Eos Trans. AGU*, *92*(28), LLNL-TR-481284, 1090004. doi: 10.1029/2011EO280002

Sanford, A., Lin, K., Tsai, I., & Jacksha, L.
Earthquake catalogs for new mexico and bordering areas: 1869–1998. .

Stankova, J., Bilek, S. L., Rowe, C. A., & Aster, R. C. (2008). Characteristics of the october 2005 microearthquake swarm and reactivation of similar event seismic swarms over decadal time periods near socorro, new mexico. *Bulletin of the Seismological Society of America*, *98*(1), 93–105. doi: https://doi.org/10.1785/0120070108

Torres, R., Snoeij, P., Geudtner, D., Bibby, D., Davidson, M., & Attema, E. e. a. (2012). Gmes sentinel-1 mission. *Remote Sensing of Environment*, *120*, 9-24. Retrieved from https://doi.org/10.1016/j.rse.2011.05.028 doi: 10.1016/j.rse.2011.05.028

Ward, K. M., Zandt, G., Beck, S. L., Christensen, D. H., & McFarlin, H. (2014). Seismic imaging of the magmatic underpinnings beneath the altiplano-puna volcanic complex from the joint inversion of surface wave dispersion and receiver functions. *Earth and Planetary Science Letters*, *404*, 43-53. doi: 10.1016/j.epsl.2014.07.022

West, M., Ni, J., Baldridge, W., Wilson, D., Aster, R., Gao, W., & Grand, S. (2004). Crust and upper mantle shear-wave structure of the southwest United States: Implications for rifting and support for high elevation. *J. Geophys. Res.*, *109*. doi: 10.1029/2003JB002575

Wilson, D., Aster, R., West, M., Ni, J., Grand, S., Gao, W., ... Patel, P. (2005, FEB 24). Lithospheric structure of the rio grande rift. *Nature*, *433*(7028), 851-855. doi: {10.1038/nature03297}

Xiao, R., Yu, C., Zhenhong, L., Song, C., & He, X. (2020). General survey of large-scale land subsidence by gacos-corrected insar stacking: Case study in north china plain. *Proc. IAHS*, *382*(213-218). Retrieved from https://doi.org/10.5194/piahs-382-213-2020 doi: 10.5194/piahs-382-213-2020

Supporting Information for "Pressurizing magma within heterogeneous crust: a case study at the Socorro Magma Body, New Mexico, USA"

Grant A. Block[1], Mousumi Roy[1], Emily Graves[2], Ronni Grapenthin[2]

[1]Department of Physics and Astronomy, University of New Mexico, 210 Yale Blvd NE, Albuquerque, 87131, NM, USA.

[2]Geophysical Institute, University of Alaska, 2156 Koyukuk Drive, Fairbanks, 99775, AK, USA.

Contents of this file

Additional Supporting Information (Files uploaded separately)

1. Large Table S3 and caption

S1. Methods - InSAR

We impose a temporal baseline of 1850 days and a perpendicular baseline of 200 m to generate interferometric pairs. Using digital elevation models with 30 meter resolution from NASA's Shuttle Radar Topography Mission (SRTM-1) elevation data (Farr & Kobrick, 2000), GMTSAR calculates terrain corrections. Removal of best-fitting bilinear ramp functions from wrapped phase images reduces background noise (e.g., tropospheric and ionospheric effects (Scott & Lohman, 2016) before unwrapping the modulo 2π radian observations into line-of-sight (LOS) displacements utilizing SNAPHU (Chen & Zebker, 2001). Mean velocity stacks are then created from individual interferograms by averaging the observed LOS deformation over the time interval of acquisition where observations are weighed by the time interval (e.g., Xiao et al., 2020). The resultant LOS velocity field map is aligned to the local GNSS stations to fit the magnitude of observations. From the average LOS deformation map, we obtain LOS profiles that transect the magma body for comparison to our finite element modeling results.

S2. Methods - Finite element models

In this work we use a finite element model built using the software package PyLith 2.2.2 (Aagaard et al., 2017). Our model is constructed within a 3D Cartesian domain with dimensions 300 km $\times$ 300 km $\times$ 200 km (Fig. S1b). The domain consists of five layers, each with a different rheology: the upper crust (UC), lower crust (LC), lithospheric mantle (LM), asthenospheric mantle (AM), and the compliant region (CR) (Fig. S1a). All of these subdomains are modeled as Maxwell linear isotropic viscoelastic materials, except for the upper crust, which is modeled as an isotropic elastic material; the parameters of these subdomains are given in Table S1. A linear meshing scheme is used on the free surface of the domain ($+z$ face) and any interface between the subdomains (e.g., the boundary between UC and LC.) The scheme sets the mesh size to its minimum (1 km) at the origin (x, y) = (0,0) of the surface and its maximum (20 km) at the edges (Fig. S1b). Outer domain boundaries other than the free surface are set to the maximum mesh size, and the faces of the magma chamber are set to the minimum mesh size. The models are benchmarked with the analytical solution for a pressurized penny shaped crack in an elastic halfspace derived by Fialko, Khazan, and Simons (2001). The radially-varying meshing scheme and overall domain size are optimized by constraining displacements to be within 10% of this analytic solution for an elastic halfspace. Models are run with a 10^{-7} relative tolerance and 10^{-9} absolute tolerance. Sensitivity analysis was conducted and we observe no change in our results when increasing the tolerances up to two orders of magnitude. The "magma chamber" in most models is represented as two spherical caps joined at their common circular edge. In the models used to fit to SMB InSAR data (Fig. 5) the magma chamber is represented as an ellipsoid with dimensions given in Table S1.

In all of our models, the pressurizing body is placed at a depth of 20 km and centered $(x, y) = (0,0)$. The radius of the source is variable, but is set to be 25 km in most cases, with the exception of the ellipsoidal source runs (Table S1). When a cylindrical low-viscosity CR is present (Fig. 2a), we consider either a uniform viscosity body ("uniform CR"), or a CR with either a lateral ("nested CR") or vertical ("stacked CR") gradient is viscosity, representing a transitional region at the edges of the CR. Viscosity variations in the nested CR and stacked CR layouts are achieved with three cylindrical subdomains. In the nested CR an inner cylinder extending the full height of the CR is surrounded by a middle cylinder with higher viscosity which in turn is surrounded by an outer cylinder with a higher viscosity (Fig. 2a, Table S1). In the stacked CR, each cylinder extends the full radius of the CR; the lowest viscosity cylinder is at the bottom, the cylinder in the middle has a higher viscosity and the highest cylinder has the highest viscosity (Fig. 2a, Table S1). In each layered CR the source is placed in the lowest viscosity subdomain. All of these layouts are developed to independently evaluate the effect of horizontal and vertical viscosity gradients around a pressurizing magma body on surface deformation.

All faces of the domain are given zero displacement Dirichlet boundary conditions with the exception of the $+z$ face, which is set to be a free surface. The pressure at the top and bottom of the magma body is given as an outward normal stress via a time dependent Neumann boundary condition, zero shear stress is specified on the magma body surfaces. The time dependence of the Neumann boundary condition is taken to be periodic after some specified "spin-up time" of constant pressure P_0 (Fig. 2b). This spin-up time is set to be 500 simulation years in all model runs, with the exception of uniform CR with models with a relaxation time of 10 years. In that case the spin-up time is set to 1000 years to give the model adequate time to equilibrate. A simulation time step of 0.1 years is specified throughout the entire model run except for runs with the 1000 year spin-up time where the time step is set to 1.5 years during the spin-up period. and the ellipsoidal source runs where the spin-up time step is set to 0.18 years. Two periodic pressure functions are used in this study, sinusoidal and "sawtooth" (Fig. 2b). The sinusoidal function is used to first understand how our models respond to periodic pressurization. It is characterized by an average pressure P_0 (the same pressure used in the spin-up period), a pressure amplitude ΔP and period T. The sawtooth function allows asymmetry with different intervals of pressurization and depressurization. It is parameterized by background pressure P_0 (again, the same pressure used in the spin-up period), pressure increase ΔP and period T. Additionally, we specify t_{rise} and t_{fall} which are the times of pressurization and depressurization respectively. Unless otherwise specified, we set $t_{rise} = 0.75T$ and $t_{fall} = 0.25T$. All pressure functions used have two cycles. Results shown are obtained from the second cycle unless noted otherwise.

To compare to the InSAR observations (Fig. 1b), surface velocity profiles from the ellipsoidal source model are rotated counterclockwise by an azimuth of -22.55° for the A-A' profile and 63.45° for the B-B' profile to match the NW-SE orientation of the long-axis of the SMB and projected onto the satellite LOS (Fig. 5c). The profiles are also horizontally displaced relative to the center of the ellipsoidal source sill, by $\Delta x \approx$ -10.0 km, $\Delta y \approx 0.5$ km (Fig 1b).

References

Aagaard, B., Knepley, M., & Williams, C. (2017). *Pylith v2.2.2 [software].* Davis, CA. doi: http://doi.org/10.5281/zenodo.438705

Aagaard, B., Williams, C., & Knepley, M. (2021, Feb). *Pylith modeling tutorial overview of cubit/trelis, pylith, and paraview.* Retrieved from https://geodynamics.org/resources/494

Chen, C. W., & Zebker, H. A. (2001). Two-dimensional phase unwrapping with use of statistical models for cost functions in nonlinear optimization. *J. Opt. Soc. Amer. A*, *18*, 338-351. doi: 10.1364/JOSAA

Farr, T. G., & Kobrick, M. (2000). Shuttle radar topography mission produces a wealth of data. *Eos Trans. AGU*, *81*, 583-583. doi: 10.1029/EO081i048p00583

Fialko, Y., Khazan, Y., & Simons, M. (2001, 07). Deformation due to a pressurized horizontal circular crack in an elastic half-space, with applications to volcano geodesy. *Geophysical Journal International*, *146*(1), 181-190. Retrieved from https://doi.org/10.1046/j.1365-246X.2001.00452.x doi: 10.1046/j.1365-246X.2001.00452.x

Scott, C., & Lohman, R. (2016). Sensitivity of earthquake source inversions to atmospheric noise and corrections of insar data. *Journal of Geophysical Research, Solid Earth*, *121*, 4031-4044. Retrieved from https://doi.org/10.1002/2016JB012969 doi: doi:10.1002/2016JB012969

Xiao, R., Yu, C., Zhenhong, L., Song, C., & He, X. (2020). General survey of large-scale land subsidence by gacos-corrected insar stacking: Case study in north china plain. *Proc. IAHS*, *382*(213-218). Retrieved from https://doi.org/10.5194/piahs-382-213-2020 doi: 10.5194/piahs-382-213-2020

S3. Table - All models

Table S1: Parameters and their values used for the models, unless otherwise noted. Regions are as in Figure S1: CR=compliant region; UC=upper crust; LC=lower crust; LM=lithospheric mantle; AM=asthenospheric mantle. The layered structure values apply for all models, except for the ellipsoidal source models where r_{source} is redefined for the x and y ellipsoidal axes and realistic V_s and V_p are assigned for each layer instead of using a constant shear modulus.

Model Type	**Parameter**	**Value**
Layered structure (background)		
	h_{UC}, UC height	10 km
	ρ_{UC}, UC density	2670 kg/m^3
	μ_{UC}, UC shear modulus	40 GPa
	h_{LC}, LC height	14 km
	ρ_{LC}, LC density	2970 km/m^3
	μ_{LC}, LC shear modulus	40 GPa
	η_{LC}, LC viscosity	1.261×10^{21} Pa s
	h_{LM}, LM height	70 km
	ρ_{LM}, LM density	3350 kg/m^3
	μ_{LM}, LM shear modulus	40 GPa
	η_{LM}, LM viscosity	1.261×10^{22} Pa s
	h_{AM}, AM height	100 km
	ρ_{AM}, AM density	3250 kg.m^3
	μ_{AM}, AM shear modulus	40 GPa
	η_{AM}, AM viscosity	1.261×10^{21} Pa s
	r_{source}, source radius	25 km
Uniform CR		
	$h_{CR,tot}$, Total CR height	14 km
	$r_{CR,tot}$, Total CR radius	50 km
	ρ_{CR}, CR density	2500 kg/m^3
	μ_{CR}, CR shear modulus	40 GPa
	η_{CR}, CR viscosity	1.261×10^{18} Pa s
Nested CR		
	$r_{CR,1}$, inner CR radius	32 km
	$r_{CR,2}$, middle CR radius	8 km
	$r_{CR,3}$, outer CR radius	10 km
	$\eta_{CR,1}$, inner CR viscosity	1.261×10^{18} Pa s
	$\eta_{CR,2}$, middle CR viscosity	1.261×10^{19} Pa s
	$\eta_{CR,3}$, outer CR viscosity	1.261×10^{20} Pa s
Stacked CR		

	$h_{CR,1}$, lower CR height	12 km
	$h_{CR,2}$, middle CR height	1 km
	$h_{CR,2}$, upper CR height	1 km
	$\eta_{CR,1}$, lower CR viscosity	1.261×10^{18} Pa s
	$\eta_{CR,2}$, middle CR viscosity	1.261×10^{19} Pa s
	$\eta_{CR,3}$, upper CR viscosity	1.261×10^{20} Pa s
Ellipsoidal Source, hybrid CR		
	$r_{source,x}$, radius of source in x direction	24 km
	$r_{source,y}$, radius of source in y direction	38 km
	$r_{CR,tot}$, total CR radius	100 km
	$h_{CR,tot}$, total CR height	14 km
	$r_{CR,1}$, inner CR radius	75 km
	$r_{CR,2}$, middle CR radius	17 km
	$r_{CR,3}$, outer CR radius	8 km
	$h_{CR,1}$, lower CR height	12 km
	$h_{CR,2}$, middle CR height	1 km
	$h_{CR,3}$, upper CR height	1 km
	$\eta_{CR,1}$, inner CR viscosity	1.261×10^{18} Pa s
	$\eta_{CR,2}$, middle CR viscosity	1.261×10^{19} Pa s
	$\eta_{CR,3}$, outer CR viscosity	1.261×10^{20} Pa s
	$V_{s,UC}$, $V_{p,UC}$, UC s and p wave speeds	3500 m/s^2, 6000 m/s^2
	$V_{s,LC}$, $V_{p,LC}$, LC s and p wave speeds	4200 m/s^2, 6500 m/s^2
	$V_{s,LM}$, $V_{p,LM}$, LM s and p wave speeds	4500 m/s^2, 7000 m/s^2
	$V_{s,AM}$, $V_{p,AM}$, AM s and p wave speeds	4300 m/s^2, 7000 m/s^2

S4. Supplementary Figures

Supplementary Figures S1 to S3.

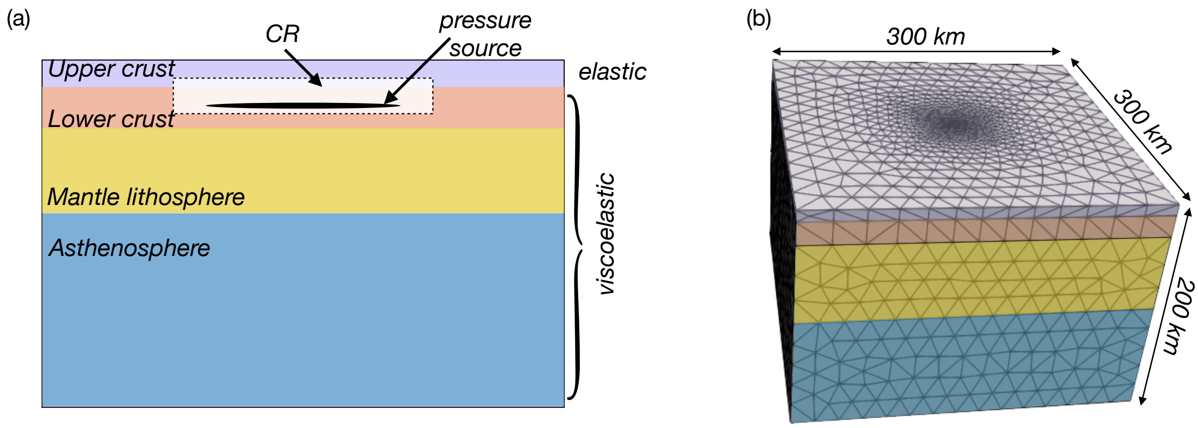

Figure S1. (a) Schematic slice of the models used in this work, composed of a background layered structure: an elastic upper crust, viscoelastic lower crust, lithospheric mantle, and asthenospheric mantle (material and geometry details in Table S1). The magma body is represented as a penny shaped or ellipsoidal pressure source at a depth of 20 km, (possibly) surrounded by a cylindrical compliant region (CR). (b) Finite-element mesh with dimensions as indicated, constructed in CUBIT/Trelis (Aagaard et al., 2021). The z=0 plane and boundaries between layers use a linear meshing scheme where element size increases radially (see Section 2).

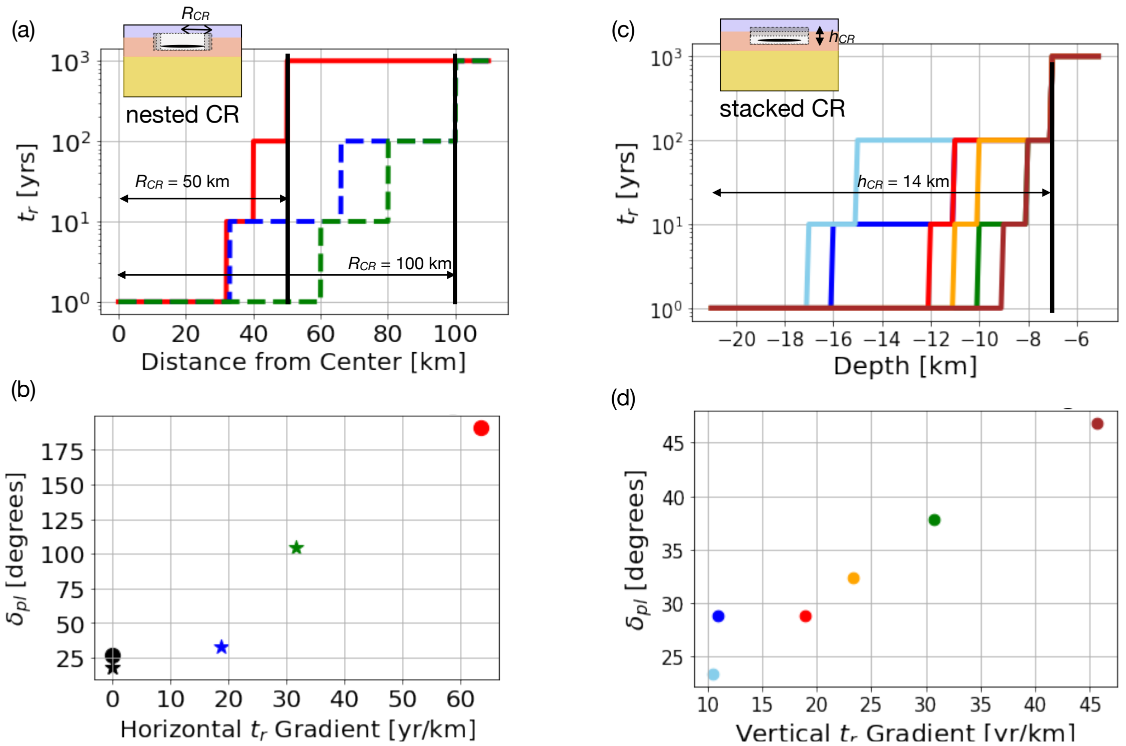

Figure S2. (a) Relaxation time vs radial distance within a model with a uniform CR (black solid lines indicate r_{CR}=50 and 100 km), and various nested CR models. The lowest relaxation time is t_r=1 yr and increases stepwise up to the ambient crustal value of t_r=10^3 yrs. Colored solid lines represent runs with r_{CR}=50 km and colored dashed lines represent runs with r_{CR}=100 km. (b) Center-shoulder phase lag calculated for sinusoidal pressure-time functions (e.g., Fig. 3 (b-d)) as a function of horizontal gradient within the various nested CR models (symbols are color-coded by the colors of the lines in (a)), and black symbols are for the uniform CR. Circles represent runs with r_{CR}=50 km and stars represent runs with r_{CR}=100 km. The model with the highest phase lag is the nested CR model in the main text. (c) Relaxation time vs depth for multiple configurations of the vertically stratified stacked CR models. The lowest relaxation time is t_r=1 yr near the source, and increases stepwise upward to the ambient crustal value of t_r=10^3 yrs. The total CR height is held constant at h_{CR} =14 km, but the layered relaxation time structure is shown for the uniform CR (solid black line) and a suite of stacked CR models. (d) Center-shoulder phase lag as a function of vertical gradient in the CR. The colors correspond to the colors used for the lines in (c).

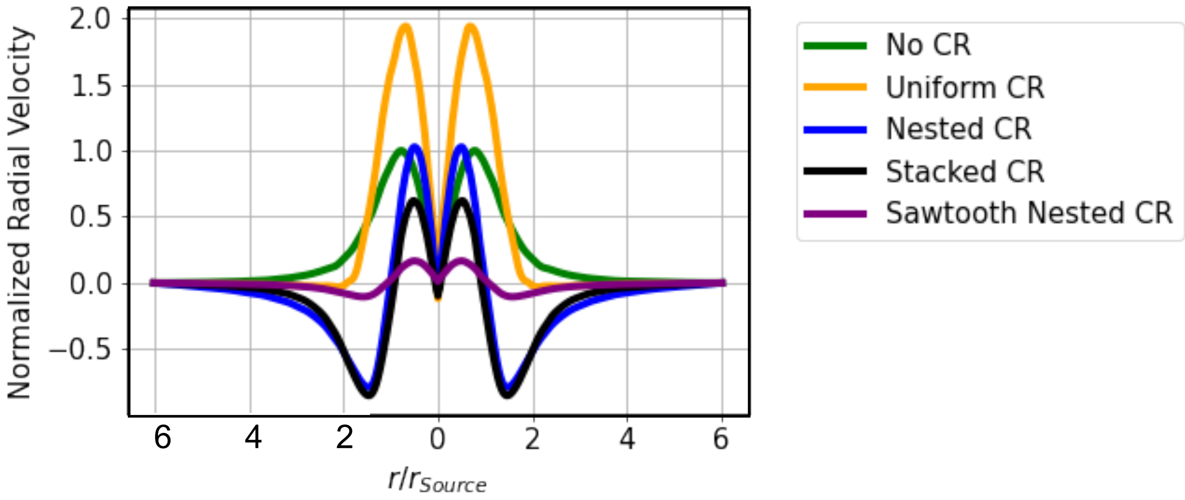

Figure S3. Normalized radial surface velocity, V_r, profiles (normalized relative to the maximum velocity of the no CR case) in four models, illustrating the role of the compliant region (CR) in the sombrero pattern of deformation. All runs shown have P_0=1MPa, ΔP=500kPa and T=200yrs. Each profile is the radial component of the runs shown in Fig. 3a, chosen at the same times as the corresponding velocity fields in Fig. 2c-f.